

---

# From Micro– to Macro–Raman Spectroscopy: Solar Silicon for a Case Study

---

George Sarau, Arne Bochmann, Renata Lewandowska and Silke Christiansen

Additional information is available at the end of the chapter

<http://dx.doi.org/10.5772/48160>

---

## 1. Introduction

The phenomenon of inelastic scattering of light by matter is referred as Raman spectroscopy named after Sir Chandrasekhara Venkata Raman who first observed it experimentally in 1928 [1]. Because only one photon out of  $10^6$ - $10^{12}$  incident photons is inelastically or Raman scattered, it took some time until lasers with high enough light intensities for efficient Raman excitation and very sensitive detectors for measuring the still low intensity Raman light were developed. Another important step in advancing Raman instrumentation was the efficient rejection of the very intense elastic scattered light, known as Rayleigh light, through a double or triple monochromator or filters [2].

Nowadays, Raman spectroscopy is being successfully applied to both in- and ex-situ analyses of various processes and materials in different states of matter (solid, liquid, gas or plasma). Moreover, Raman spectrometers have become small, portable and easy to use even for nonspecialists. This technique is covering a very broad range of application fields, at scientific and industrial levels, including pharmaceuticals, biology, environment, forensics, geology, art, archaeology, catalysis, corrosion, materials and others. Giving the large amount of specific information related to each of the abovementioned areas, we refer the interested reader to [3,4].

In the field of semiconductors, Raman spectroscopy has shown to be a powerful analytic tool for investigating mechanical stress, crystallographic orientation, doping, composition, phase, and crystallinity of semiconductor materials in bulk, thin film and device form [4-7]. In particular, the use of Raman spectroscopy to study solar silicon materials in form of thin films on glass, wafers, and ribbons, which are then processed to solar cells used as a clean and sustainable energy source has gained new momentum in the context of climate change and energy security. The physics behind Raman scattering in semiconductors or crystals is based on the inelastic interaction of light with lattice vibrations or phonons that are sensitive

---

to internal and external perturbations. A short but relevant theoretical introduction in the case of silicon will be given in Section 2. Back to early 70th, it was Anastassakis et. al. first reporting on the shift of the first-order silicon Raman peak under uniaxial *external* stress [8]. This work triggered the application of Raman spectroscopy in measuring *internal* stresses present in semiconductor materials and structures. Particularly important for the present contribution are the studies on *local* internal stresses in microelectronics devices such as silicon integrated circuits using confocal micro-Raman spectroscopy where the exciting laser light is focused onto the sample's surface through a microscope objective thus enabling investigations on the micrometer scale [4,5].

The first experimental part of this chapter (Sections 3.2 and 4.1) is mainly focused on the application of confocal *micro-Raman spectroscopy* to map the spatial distribution of internal stresses, their magnitude and sign in different solar silicon materials following the existing work in silicon microelectronics. Because internal stresses may decrease mechanical strength increasing the breakage rate and induce recombination active defects when combined with external stresses, their understanding and control will improve both process yields and solar cell efficiencies. In addition to mechanical information, other useful material properties can be obtained from the *same* first-order silicon Raman peak. We will show how internal stresses, defects, doping, and microstructure can be directly correlated with each other on the same map, enabling the basic understanding of their interactions. The micro-Raman measurements are supported and complemented at identical positions by other techniques such as EBSD, EBIC, and defect etching. Such a combination allows the correlation of internal stresses, recombination activity and microstructure on the micrometer scale.

In the second experimental part of this contribution (Sections 3.3 and 4.2), confocal *macro-Raman spectroscopy* is introduced and its application to solar silicon is demonstrated for the first time. Macro-Raman spectroscopy represents the state-of-the-art in fast, large area Raman mapping being initially developed to analyze the chemical homogeneity in pharmaceutical tablets. We will present a statistical analysis using Macro-Raman mapping of solar silicon, which is usually characterized by large spatial properties variations. The combination of the two mapping techniques offers insights into the interplay between solar silicon properties at different length scales. Finally, the potential use of macro-Raman spectroscopy for optimization and in-line quality check in a PV factory will be discussed.

Such detailed Raman studies are not limited to solar silicon materials but they can be performed on all Raman active materials. In this context, it is clear that today Raman spectroscopy is a versatile and mature characterization method, which can be applied both at micro- and macro-scale to learn about the interaction between materials properties and their optimization in relation to individual processing steps.

## 2. Theoretical background of Raman spectroscopy in silicon

The aim of this section is to provide the basic equations and their interpretation necessary to understand the experimental results shown throughout the present chapter. A rigorous mathematical derivation is extensively documented in many textbooks and papers published during the long history of the Raman effect [4,5,8-14].

In a Raman experiment described from a classical point of view, monochromatic light of frequency  $\omega_i$  originating from a laser is incident on a crystal in a direction  $\mathbf{k}_i$  with  $\mathbf{E} = E_0 \exp[i(\mathbf{k}_i \cdot \mathbf{r} - \omega_i t)]$ . The electric field of light will induce an electric moment  $\mathbf{P} = \varepsilon_0 \chi \mathbf{E}$ , with the interaction between light and crystal at position  $\mathbf{r}$  being mediated by lattice vibrations or phonons characterized by a wavevector  $\mathbf{q}_j$  and a frequency  $\omega_j$  with  $Q_j = A_j \exp[\pm i(\mathbf{q}_j \cdot \mathbf{r} - \omega_j t)]$ . It is the electrical susceptibility  $\chi$ , which is changed by phonons. This means that the induced electric moment will emit besides the elastic scattered Rayleigh light of  $\omega_i$ , Raman light of  $\omega_i + \omega_j$  and  $\omega_i - \omega_j$  resulting from anti-Stokes and Stokes Raman scattering, respectively [5]:

$$\mathbf{P} = \varepsilon_0 \chi_0 \cdot \mathbf{E}_0 \exp[i(\mathbf{k}_i \cdot \mathbf{r} - \omega_i t)] + \varepsilon_0 \mathbf{E}_0 \left( \frac{\partial \chi}{\partial Q_j} \right)_0 A_j \times \exp[-i(\omega_i \pm \omega_j)t] \exp[i(\mathbf{k}_i \pm \mathbf{q}_j) \cdot \mathbf{r}]. \quad (1)$$

From a quantum mechanical point of view, a photon described by  $\mathbf{k}_i$ ,  $\omega_i$  produces an electron-hole pair. The electron is excited from the ground state to a higher energy state and interacts with a phonon characterized by  $\mathbf{q}_j$ ,  $\omega_j$ . As a result of this interaction, the electron gains or losses energy and through the recombination of the electron-hole pair a photon  $\mathbf{k}_s$ ,  $\omega_s$  is emitted, where  $\omega_s = \omega_i + \omega_j$  and  $\omega_s = \omega_i - \omega_j$  for anti-Stokes and Stokes Raman scattering, respectively. In most cases, only the silicon Stokes Raman peak known also as the first-order silicon Raman peak occurring in the absence of internal and external perturbations at  $\omega_0 \sim 520 \text{ cm}^{-1}$  is measured and examined. This peak is referred as the silicon Raman peak throughout the next sections. It corresponds to lower energy scattered photons  $\lambda_1$  than the incident ones  $\lambda_0$ . The conversion formula from nm to  $\text{cm}^{-1}$  is written as:

$$\Delta\omega(\text{cm}^{-1}) = \left( \frac{1}{\lambda_0(\text{nm})} - \frac{1}{\lambda_1(\text{nm})} \right) \times 10^7. \quad (2)$$

## 2.1. Orientation evaluation

The Raman scattering efficiency or intensity depends on the polarization direction of the incident ( $\mathbf{e}_i$ ) and backscattered ( $\mathbf{e}_s$ ) light and on the three silicon Raman tensors  $\mathbf{R}_j$  which are proportional to  $(\partial\chi/\partial Q_j)_0$  (see Equation 1),  $I_0$  is a constant including all fixed experimental parameters [5,10,14]:

$$I(\mathbf{e}_i, \mathbf{e}_s) \approx I_0 \cdot \sum_{j=1}^3 \left| \mathbf{e}_i \cdot \mathbf{R}_j \cdot \mathbf{e}_s \right|^2. \quad (3)$$

Here the polarization directions are defined in the stage coordinate system, while the Raman tensors refer to the crystal coordinate system. The crystal - stage transformation is performed by means of a rotation matrix  $\mathbf{T}(\alpha, \beta, \gamma)$  applied to the Raman tensors  $\mathbf{R}_j$ , where  $\alpha$ ,  $\beta$ , and  $\gamma$  are the three Euler angles [10]:

$$I(\mathbf{e}_i, \mathbf{e}_s) \approx I_0 \cdot \sum_{j=1}^3 \left| \mathbf{e}_i \cdot \left( \mathbf{T}^{-1}(\alpha, \beta, \gamma) \cdot \mathbf{R}_j \cdot \mathbf{T}(\alpha, \beta, \gamma) \right) \cdot \mathbf{e}_s \right|^2. \quad (4)$$

By continuously rotating the polarization direction of the incident laser light  $\theta$  with a  $\lambda/2$  plate for two analyzer positions  $x$  and  $y$ , it is possible to obtain two experimental curves showing the intensity variations of the silicon Raman peak. The data fitting based on Equation (4) results in the numerical evaluation of the three Euler angles which are needed to describe the crystallographic orientation of a particular grain with respect to the stage (reference) coordinate system. Having the grain orientation, the intensity variations of the three optical phonons with polarization settings  $I_x^j(\theta)$  and  $I_y^j(\theta)$  can be simulated separately. These six intensity variations can be transformed into six intensity ratio functions [10]:

$$W_1^{x,y}(\theta) = \frac{I_1^{x,y}(\theta)}{I_2^{x,y}(\theta) + I_3^{x,y}(\theta)}, W_2^{x,y}(\theta) = \frac{I_2^{x,y}(\theta)}{I_1^{x,y}(\theta) + I_3^{x,y}(\theta)}, W_3^{x,y}(\theta) = \frac{I_3^{x,y}(\theta)}{I_1^{x,y}(\theta) + I_2^{x,y}(\theta)} \quad (5)$$

It has been shown that for almost any arbitrary oriented grain, distinct polarization settings ( $\theta$ ,  $x$  or  $y$ ) for which the intensity of one phonon prevails over the intensity sum of the other two phonons can be found [10]. Performing three Raman measurements on the same grain, one for every single-phonon polarization settings, several stress tensor components can be determined as experimentally shown in Section 4.1.1.

## 2.2. Stress evaluation

In the absence of stress (internal or external), the three Raman optical phonons of silicon are degenerate leading to a single Raman peak at  $\omega_0 \sim 520 \text{ cm}^{-1}$ . Large mechanical stresses in the GPa range lift the degeneracy causing frequency shifts of the three optical phonons  $\Delta\omega_j = \omega_j - \omega_0$ , which appear as separate peaks in the Raman spectrum depending on the direction of the applied stress and measurement conditions [8,12,13]. When the stress level is below 1 GPa, these frequency shifts are too small to be resolved being masked by the natural width of the silicon Raman peak. In such cases, particular polarization settings for the incident and backscattered Raman light can be found that allow the excitation and probing of the three optical phonons almost separately and consequently their frequency shifts can be determined. These settings vary with the orientation of the investigated grain as discussed in the previous section. Next step consists in using the secular equation that relates the frequency shifts to the strain tensor components [5,9,10]:

$$\begin{vmatrix} p \cdot \varepsilon'_{xx} + q \cdot (\varepsilon'_{yy} + \varepsilon'_{zz}) - \lambda & 2r \cdot \varepsilon'_{xy} & 2r \cdot \varepsilon'_{xz} \\ 2r \cdot \varepsilon'_{xy} & p \cdot \varepsilon'_{yy} + q \cdot (\varepsilon'_{xx} + \varepsilon'_{zz}) - \lambda & 2r \cdot \varepsilon'_{yz} \\ 2r \cdot \varepsilon'_{xz} & 2r \cdot \varepsilon'_{yz} & p \cdot \varepsilon'_{zz} + q \cdot (\varepsilon'_{xx} + \varepsilon'_{yy}) - \lambda \end{vmatrix} = 0. \quad (6)$$

Here  $p$ ,  $q$ , and  $r$  are material constants so-called phonon deformation potentials being the only three independent components for cubic symmetry crystals such as silicon,  $\varepsilon'_{ij}$  are the strain tensor components in the crystal coordinate system, while the eigenvalues  $\lambda_j$  ( $j = 1,2,3$ ) are given by

$$\lambda_j = \omega_j^2 - \omega_0^2 = (\omega_j - \omega_0) \cdot (\omega_j + \omega_0) \approx \Delta\omega_j \cdot 2\omega_0. \quad (7)$$

The stress tensor components are finally obtained from the inverse Hooke's law  $\varepsilon'_{ij} = S_{ij} \cdot \sigma'_{ij}$  where  $S_{ij}$  represents the elastic compliance tensor whose components are material constants. It is evident from Equation (6,7) that the three frequency shifts  $\Delta\omega_j$  are not enough to determine the six independent stress tensor components  $\sigma'_{ij}$ . The probing depth in silicon ranges from a few hundreds of nm to a few  $\mu\text{m}$  for visible excitations, and from a few nm to a few tenths of nm for UV excitations. Thus, due to wavelength dependent absorption, only the stress state close to the sample's surface is measured. This implies a predominant planar stress state described by three stress components  $\sigma'_{xx}$ ,  $\sigma'_{yy}$ , and  $\tau'_{xy}$  that can be numerically evaluated using the three frequency shifts  $\Delta\omega_j$ . The residual stress components in the z direction given by  $\sigma'_{zz}$ ,  $\tau'_{xz}$ , and  $\tau'_{yz}$  are included in  $\Delta'_z$  which also serves as a correction parameter [10]:

$$\sigma' = \begin{pmatrix} \sigma'_{xx} & \tau'_{xy} & 0 \\ \tau'_{xy} & \sigma'_{yy} & 0 \\ 0 & 0 & \Delta'_z \end{pmatrix}. \quad (8)$$

The following equation can be used to transform the stress tensor components into average or von Misses stress:

$$\sigma'_{av} = \sqrt{\sigma'^2_x + \sigma'^2_y + \sigma'^2_z - \sigma'_x \sigma'_y - \sigma'_x \sigma'_z - \sigma'_y \sigma'_z + 3(\tau'^2_{xy} + \tau'^2_{xz} + \tau'^2_{yz})} \quad (9)$$

Another more straightforward way to relate measured Raman shifts to stress values is the use of a simple stress model illustrating the stress state in the sample. The classical example in the case of silicon is the presence of uniaxial stress  $\sigma$  along the [100] direction and the measurement of the backscattered Raman signal from the (001) surface [5]. In this configuration, only one stress tensor component is non zero:

$$\Delta\omega_3 (cm^{-1}) = -2 \cdot 10^{-9} \sigma (Pa) \text{ or } \sigma (MPa) = -500 \times \Delta\omega (cm^{-1}). \quad (10)$$

If biaxial stress in the x-y plane with stress components  $\sigma_{xx}$  and  $\sigma_{yy}$  (or  $\sigma_{xx} = \sigma_{yy}$  for isotropic stress) describes the stress distribution in the sample:

$$\Delta\omega_3 (cm^{-1}) = -4 \cdot 10^{-9} \left( \frac{\sigma_{xx} + \sigma_{yy}}{2} \right) (Pa) \text{ or } \sigma_{xx} = \sigma_{yy} (MPa) = -250 \times \Delta\omega (cm^{-1}). \quad (11)$$

These two formulas (10,11) written in the stage coordinate system are commonly used in the community for a fast and reliable estimation of the *average stress* independently of the crystallographic orientation of grains in multicrystalline silicon. Thus, 1  $\text{cm}^{-1}$  shift of the silicon Raman peak with respect to the stress free value of  $\sim 520 \text{ cm}^{-1}$  corresponds to a uniaxial stress of 500 MPa or to a biaxial in-plane isotropic stress of 250 MPa. It can be seen that tensile stress shifts the silicon Raman peak to lower frequency, while compressive stress to higher frequency as sketched in Figure 1(a). Experimental examples of the stress state evaluation using both methods described above will be given in Section 4.1.

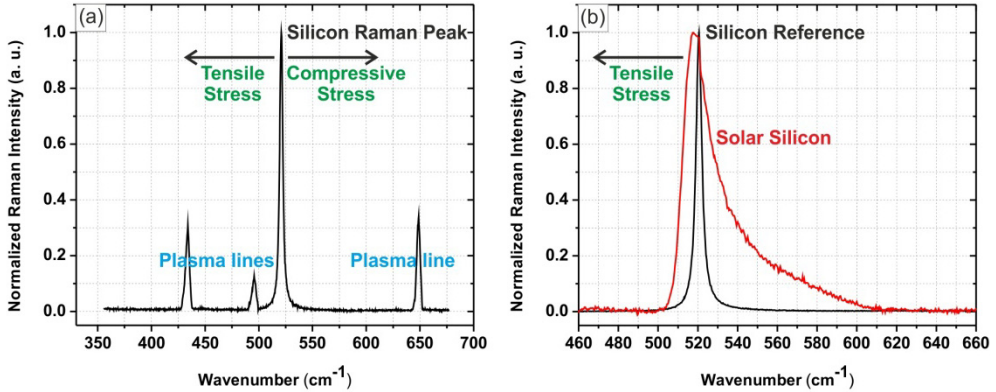


**Figure 1.** (a) Typical Raman spectrum of a silicon wafer used as reference. In the absence of stress, the three Raman optical phonons of silicon ( $1 \times \text{LO}$ ,  $2 \times \text{TO}$ ) are degenerate resulting in a single Raman peak at  $\omega_0 \sim 520 \text{ cm}^{-1}$ . The plasma lines originating from an external reference lamp are used to correct the silicon peak position with respect to the thermal drift of the spectrometer grating. Tensile or compressive stresses (internal or external) below 1 GPa may shift the silicon Raman peak to lower or higher frequencies, respectively. (b) Comparison between Raman spectra of stress-free silicon reference and tensile stressed thin film solar silicon on glass. The peak asymmetry caused by high boron doping is clearly visible.

### 2.3. Doping evaluation

In the case of highly doped silicon, a resonant interaction occurs between the discrete optical phonon states (phonon Raman scattering) and the continuum of electronic states in the valence or conduction bands (electronic Raman scattering) because of electron-phonon coupling. This leads to Fano-type silicon Raman peak asymmetries, which can be observed as tails either on the right side (for p-type doping) or on the left side (for n-type doping) of the otherwise symmetric silicon Raman peak as shown in Figure 1(b) [11,14-17]. The function used to fit the intensity of the silicon Raman peak  $I(\omega)$  is given by [11]

$$I(\omega, q, \Gamma, \omega_{\max}) = I_0 \frac{[q + 2(\omega - \omega_{\max}) / \Gamma]^2}{1 + [2(\omega - \omega_{\max}) / \Gamma]^2}. \quad (12)$$

Here  $I_0$  is a scaling factor,  $q$  is so-called symmetry parameter,  $\Gamma$  is the linewidth of the peak, and  $\omega_{\max}$  is the peak position in the presence of Fano interaction. The symmetry parameter  $q$  describes the shape of the silicon Raman peak affected by Fano resonances. Large  $q > 150$  values correspond to standard doping ( $< 10^{16} \text{ cm}^{-3}$ ) resulting in a nearly symmetric peak, while small  $q < 50$  values correlate with high doping ( $> 10^{18} \text{ cm}^{-3}$ ) and pronounced peak asymmetry. For highly doped silicon,  $1/q$  is approximately proportional to the free carrier concentration [11]. Thus, an accurate quantitative evaluation of doping on the micrometer scale is possible, provided a good calibration curve exist.

## 2.4. Qualitative defect density evaluation

As shown in the previous three sections, Raman spectroscopy can provide detailed information about semiconductor materials, in this contribution solar silicon, including crystal orientation, internal stresses and doping, which can be extracted from the intensity, position and asymmetry of the silicon Raman peak. In addition, the linewidth of the peak relates to the presence of extended crystal defects. In a perfect crystal, the phonon lifetimes are theoretically infinite in the harmonic approximation that neglects third- and higher-order derivatives of the crystalline potential resulting in narrow delta function-like linewidths of the optical phonon Raman spectra [18]. Defects act as anharmonic perturbations leading to finite phonon lifetimes that manifest themselves as a broadening of the peak described by its full-width at half maximum denoted FWHM or  $\Gamma$ . Therefore, the anharmonic lifetimes of phonons are defined as  $1/\Gamma$  being evaluated using first principles calculations including both kinematic effects; i.e., the decay of phonons into vibrations of lower frequency and dynamic effects; i.e., the magnitude of the tensor of the third derivatives of the crystal potential with respect to atomic displacements that describes the instability of one-phonon states. The calculated  $\Gamma$  values of the Raman-active optical phonons were found to agree well with those determined experimentally in the case of single crystalline semiconductors (defect free) such as diamond, Si, Ge, GaAs, GaP and InP [19,20].

Anharmonic effects and consequently broadening can also be induced by internal or external stresses approaching the stress-induced splitting limit of the peak as discussed in Section 2.2 or by large stress gradients within the probed volume [5]. Moreover, doping and/or impurities can either produce new Raman peaks through their own vibrational modes or alter/broaden the Raman spectrum of the host material through the change in mass and bond length (atomic effects) as well as through the resonant Fano interaction of free carriers (donors or acceptors) with the lattice (electronic effects). Because all these information originates from the silicon Raman peak, one can separate between the effects of stresses, doping and/or impurities and that of defects on the FWHM values. The Raman linewidths were also found to broaden in the case of relatively small grains (in the nm range) due to the phonon confinement effect, that is, the frequency distribution of the scattered light comes from a broader interval in  $k$ -space around the  $\Gamma$ -point in the Brillouin-zone since the  $\Delta k = 0$  selection rule is partially lifted by the phonon scattering at grain boundaries [21]. Such a broadening does not occur in large grained solar silicon as presented here.

## 3. Experimental details

### 3.1. Sample preparation for Raman measurements

Raman spectroscopy investigates materials nondestructively, the appropriate excitation laser power to avoid damage being material dependent, without elaborated sample preparation. In the case of silicon thin film solar cells on glass, no sample preparation is needed because the as-grown material has low roughness. This is different for wafer- and

ribbon-based solar cells for which a simple sample preparation procedure is necessary. Their surfaces have to be evened out by mechanical polishing prior to the Raman measurements to avoid artifacts induced by uncontrolled reflections at rough surface facets. The standard polishing procedure applied to small pieces consists in changing gradually from larger to smaller diamond particle sizes with the final polishing step removing most of the previously damage surface layer, thus leaving the samples in a negligible polishing-induced stress state. The cutting into small pieces leads to stress relaxation due to the creation of free surfaces as discussed in Section 4.1.2. After polishing, the samples are Secco-etched [22] for 5 seconds to make the grain boundaries and dislocations visible. This short defect etching step does not affect the Raman scattering or the other measurement techniques used herein.

### 3.2. Micro-Raman spectroscopy

The incident light needed for Raman excitation is provided by a laser with a main emission with narrow line width. An interferential filter is used to block the other emissions of the laser. After being reflected by an edge or a notch filter, the light is focused onto the sample's surface through a microscope objective, thus giving rise to the term micro-Raman spectroscopy. Depending on the objective (magnification, numerical aperture) as well as on the excitation wavelength, the diameter of the incident laser beam is different. For the 100x objective (numerical aperture 0.9) and 633 nm excitation employed in the micro-Raman measurements presented here, the probing diameter is  $\sim 1 \mu\text{m}$ . The laser power density can be quite high, thus a low laser power of  $\sim 2 \text{ mW}$  at the silicon sample's surface should be used. In these conditions, no shift or increase in the FWHM of the silicon Raman peak due to the local heating of the sample by the laser beam were observed.

As already mentioned in Section 2.2, the probing depth is controlled by the material absorption, which is wavelength dependent. In crystalline silicon, an excitation wavelength of 633 nm results in a penetration depth of  $\sim 3 \mu\text{m}$ , while 457 nm gives  $\sim 300 \text{ nm}$ . Since we use 633 nm, the entire thickness of the silicon thin films on glass is probed, while only the surface of the  $\sim 200 - 250 \mu\text{m}$  thick silicon wafers and ribbons is measured. The backscattered Raman light passes back through an edge or a notch filter which cuts most of the Rayleigh light, it is dispersed using a grating and then detected by a silicon CCD detector. All Raman measurements herein were performed at room temperature in the backscattering configuration using a LabRam HR800 spectrometer from Horiba Jobin Yvon. A schematic picture of our micro-Raman spectrometer is displayed in Figure 2.

In order to draw correct conclusions about materials with varying spatial properties, not only several but many Raman spectra are acquired while moving the microscope stage with the sample in  $x$ - and  $y$ -directions in steps equal or smaller than the diameter of the laser probing beam as shown in Figure 2. This results in a complete micro-Raman mapping of the investigated areas, which are usually in the range of a few tens of  $\mu\text{m}^2$ . The exposure time is typically up to 1 s per spectrum. These spectra are fitted with a Gauss-Lorentzian function and maps of the shift, FWHM and intensity of the silicon Raman peak corresponding to the spatial distributions of internal stress, defect density and grain orientation are obtained. A Fano-like



fitting function as in Equation 12 is used for doping evaluation [11]. To ensure correct interpretation of the Raman data as well as to be able to visualize small mechanical stresses, the effect of the thermal drift of the spectrometer grating on the silicon peak position is corrected [5,14]. This is done by using one of the plasma lines visible in Figure 1(a) emitted by an external lamp located either close to the spectrometer's confocal hole or above the microscope [23,24].

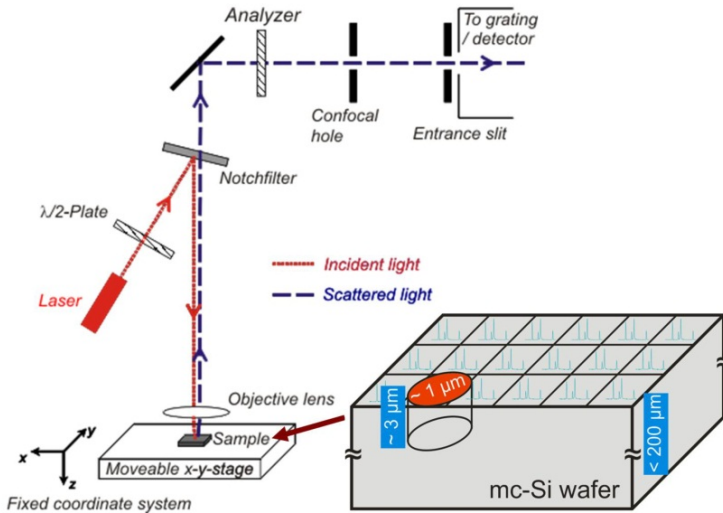


**Figure 2.** Schematic picture of the used micro-Raman spectrometer. The  $\lambda/2$  plate and the analyzer adjust the polarization direction of the incident and backscattered light with respect to the stage (fixed) coordinate system. The polarized micro-Raman procedure enables the evaluation of the crystallographic orientation of arbitrary grains and of stress components as described in Sections 2.1 and 2.2. A graphical representation of micro-Raman mapping obtained by moving the microscope stage with the sample (multicrystalline silicon wafer) in  $x$ - and  $y$ -directions under a 633 nm exciting laser along with the Raman probing volume are also shown.

### 3.3. Macro-Raman spectroscopy

Macro-Raman spectroscopy enables fast, large area Raman mapping in the  $\text{cm}^2$  range needed for statistical studies of materials properties and the correlations between them and with processing. In the context of PV, this technique can be used not only for fundamental studies in laboratory scientific research but also for optimization and in-line quality check in a PV factory. Macro-Raman mapping is possible through two add-ons that can be integrated in any existing micro-Raman spectrometer. The two new DuoScan™ (hardware) and SWIFT™ (software) Raman scanning modules developed by HORIBA Jobin Yvon provide significant reduction by orders of magnitude of the measurement times by means of large area probing beam (macro-beam) and high speed detector-stage coordination, respectively. Even faster Raman imaging is possible by combing these two technologies [7].

DuoScan™ Raman imaging technology extends the imaging capabilities of micro-Raman instruments from (sub-) micron to macro-scale mapping. The integration of the DuoScan

unit to an existing micro-Raman spectrometer is shown in Figure 3(left). This mode is based on a combination of two orthogonally rotating piezo-mirrors that scan the laser beam across the sample following a user-defined pattern as displayed in Figure 3(middle). The size of the resulting macro-beam is adjustable being limited only by the opening of the used microscope objective. The maximum macro-beam sizes achievable with our 50x (NA 0.80) or 10x (NA 0.30) NIKON microscope objectives are  $100 \times 100 \mu\text{m}^2$  or  $1 \times 1 \text{mm}^2$ . DuoScan allows to integrate the Raman signal over the macro-beam area giving an average spectrum, which contains the same spectral information as that obtained by averaging all micro-Raman spectra for the same area. The gain in acquisition time is evident, macro-Raman being orders of magnitude faster than conventional micro-Raman. For example, if an area of  $30 \times 30 \mu\text{m}^2$  is entirely probed by macro-Raman in one second, micro-Raman with a spot-size of  $1 \times 1 \mu\text{m}^2$  needs 900 seconds to cover the same area. The price one has to pay is the loss of lateral resolution.

Furthermore, DuoScan can be used in a step-by-step mode where the mapping takes place without moving the stage with the sample. A minimum step size of 50 nm is reached by deflecting the laser beam, which complements successfully the stepping capability of the stage specified to be  $\sim 500 \text{nm}$ . This mode applies for Raman imaging of nanoscale objects and features. The DuoScan mapping capabilities are summarized in Figure 3(right).

SWIFT™ Raman imaging technology enables ultra fast mapping without losing lateral resolution and thus image quality. In this mode, the time intervals needed for the stage to accelerate/decelerate as well as for the shutter in front of the detector to open/close for each measurement point are eliminated. Basically, these are dead times, which are not used for the acquisition of the Raman signal. The breakthrough consists in continuously moving the stage with the sample while keeping the shutter open and measuring continuously Raman spectra by means of high speed detector-stage coordination coupled with the high optical throughput of the Raman system. The SWIFT option can also be used for time resolved Raman imaging provided the investigated processes occur on the measurement time scale.

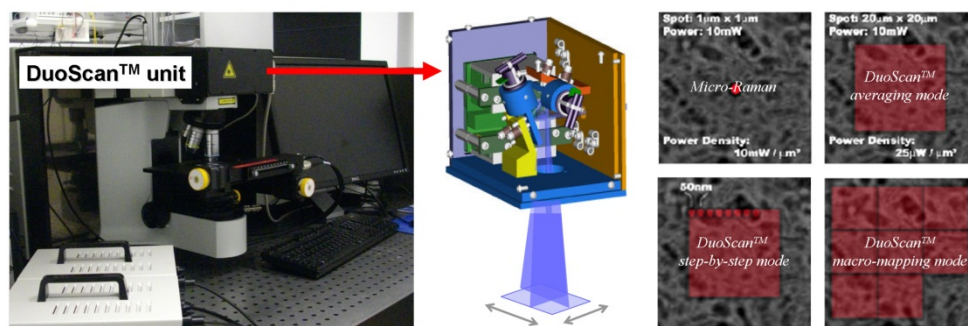


**Figure 3.** (left) DuoScan unit attached to a micro-Raman spectrometer. (middle) Schematic drawing illustrating the DuoScan working principle. The probing micro-beam is scanned by two orthogonally rotating piezo-mirrors resulting in a macro-beam, thus giving rise to the term macro-Raman spectroscopy. (right) Comparison between standard and DuoScan mapping modes described in the text. The left and middle pictures are taken from HORIBA's official webpage.

### 3.4. Complementary techniques to Raman spectroscopy for solar silicon studies

The Raman investigations on semiconductor materials represent an important step towards their fundamental understanding and the control of their properties for designing devices with specific functions. As already mentioned, Raman spectroscopy can provide detailed information regarding the spatial distributions of internal stress, defect density, doping, and grain orientation. We will show that even more insight into the interaction between different properties of silicon PV materials can be achieved when Raman measurements are supported and complemented at identical positions by other techniques such as EBSD, EBIC and defect etching.

EBSD measurements are performed using an EDAX system attached to a TESCAN LYRA XMU scanning electron microscope (SEM) to determine the grain orientations and grain boundary types. The crystal orientation is given in the  $\{hkl\}\langle uvw \rangle$  representation where  $\{hkl\}$  is the crystal plane perpendicular to the sample normal direction (z axis) and  $\langle uvw \rangle$  is the crystal direction aligned with the transverse direction of the sample (y axis). The inverse pole figure (unit triangle) shows the sample normal direction relative to the axes of the measured crystal. The misorientation between adjacent grains is given in the angle/axis notation, that is, the rotation angle about the axis common to both lattices to bring them into coincidence, and in terms of  $\Sigma$ -value which denotes the fraction of atoms in the GB plane coincident in both lattices [25].

EBIC measurements are done with an EVO 40 SEM at 20 keV beam energy both at room temperature and 80K to image most of the electrically active defects. In order to render the inhomogeneities of recombination clearly visible, a color scale is used for the EBIC maps. The maps represent the local EBIC signal normalized by the maximum EBIC signal. The lower the EBIC signal, the higher the recombination activity.

## 4. Results and discussions

### 4.1. Micro-Raman measurements

#### 4.1.1. Silicon thin films on glass for solar cells

The unique characterization power of the Raman technique consists in the detailed mechanical and microstructural information that can be extracted from the silicon Raman peak: (1) the peak position map - the distribution, amount and sign of internal stresses, (2) the peak full-width at half maximum (FWHM) map - the distribution and qualitative comparison of defect densities, (3) the peak asymmetry map - the distribution and amount of doping, and (4) the peak intensity map - the grain orientation and the grain boundary pattern [7,10,11].

One representative example is shown in Figure 4 for the laser crystallized silicon seed layers of thin film solar cells on glass (in this example, 110 nm thick silicon seed film). The larger FWHM values in Figure 4(a) indicating a broadening of the Raman spectra are produced by a decrease in the phonon lifetimes, which in turn is mainly due to defects acting as

anharmonic perturbations (see Section 2.3). Indeed, the dashed line contours in Figure 4(a) corresponds to low angle GBs indicated by arrows in the EBSD maps shown in Figure 4(e and f). It is well known that low angle GBs consist of dislocation networks/arrays. Their presence at these positions is further supported by the continuously changing crystallographic orientation within the studied grain as indicated by the gradual changing color in the intergranular misorientation gradient map by EBSD in Figure 4(f). Such intergranular misorientation is attributed to geometrically necessary dislocations forming low angle GBs [26].

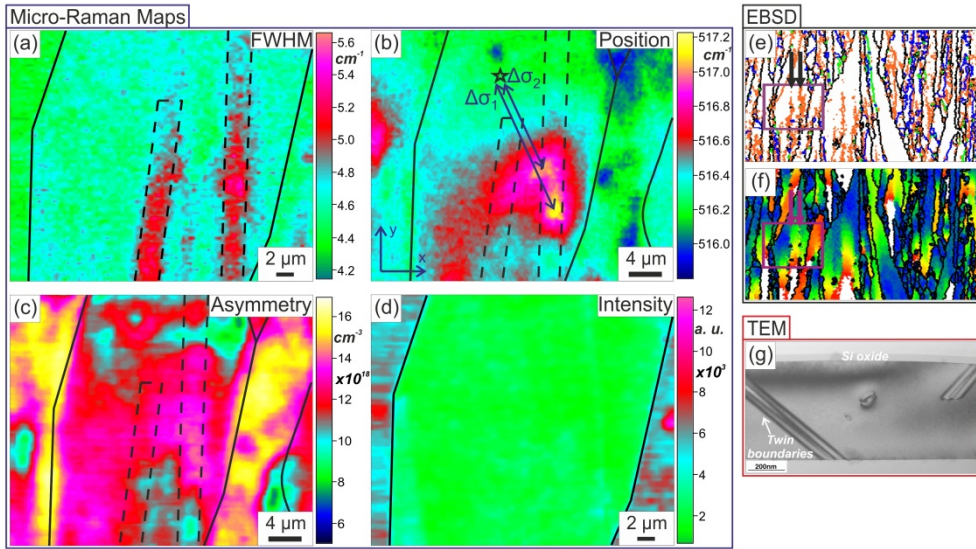


**Figure 4.** Micro-Raman maps of a laser crystallized silicon seed layer of a thin film solar cell on glass (110 nm thick, nominal boron doping of  $2.1 \times 10^{19} \text{ cm}^{-3}$ ) obtained from the fitting of the first-order Raman spectra of silicon: (a) peak FWHM – defect density map, (b) peak position – internal stress map with two lateral stress gradients  $\Delta\sigma_1=227$ ,  $\Delta\sigma_2=197 \pm 12 \text{ MPa}$  (von Mises stresses), (c) peak asymmetry – doping map, (d) peak intensity – grain orientation map. EBSD maps: (e) grain boundary map including high angle GBs (black lines), low angle GBs (orange lines),  $\Sigma 3$  GBs (blue lines),  $\Sigma 9$  GBs (green lines), (f) Intergranular misorientation gradient map. The two vertical arrows indicate low angle GBs corresponding to the areas delineating by dashed lines in (a, b and c). (g) TEM cross-section image.

Dislocations are considered to be among the most detrimental type of defect controlling not only the mechanical but also the electrical properties of silicon and other materials. They are produced by the partial or total relaxation of thermally induced stresses during the crystallization and cooling processes as long as plastic deformation is allowed by temperature, this means above the brittle-ductile transition temperature of silicon. Below this temperature, the remaining thermally induced stresses are incorporated as thermally induced residual stresses in the silicon material. Once created, dislocations can move on glide planes leading to further plastic deformation through their multiplication until the lattice friction becomes larger than the effective stress needed for moving the existing dislocations [6].

By comparing the FWHM (defect density) and position (stress) maps displayed in Figure 4(a and b), it can be seen that the two patterns are unlike. Regions of similar FWHM values (similar defect densities) along the two lines of dislocations exhibit different Raman peak positions (different stress levels) showing virtually no influence of internal stresses on peak broadening. The fact that the two dislocation lines are only partly accompanied by stress can be explained by the locally different superposition of stress fields of dislocations and thermally induced residual stresses. Their interaction can lead to local configurations in which internal stresses get cancelled totally, partially or not at all [6,23,27]. Thus, we attribute the stress concentrations in Figure 4(b) to particular combinations of (1) defect configurations/structures, which do not necessary result in higher FWHM values and (2) thermally induced residual stresses. The stress map is corrected for the compressive contributions produced by the Fano effect and by the addition of boron by means of the lattice parameter using Vergard's law [7]. The presence of different types of defects and their nonuniform distribution inside the laser crystallized seed layer are supported by transmission electron microscopy (TEM) investigations shown in Figure 4(g).

Two lateral stress gradients inside the central grain in Figure 4(b) are evaluated in form of stress-tensors following the polarized micro-Raman procedure described in [10]. First, the crystallographic grain orientation is determined using the Raman intensity dependences on the polarization direction of the incident light ( $\theta$ ) and Raman backscattered light ( $x$  or  $y$  analyzer positions) as explained in Section 2.1 at the point marked by the star within this particular grain. The measured plots are displayed in Figure 5.

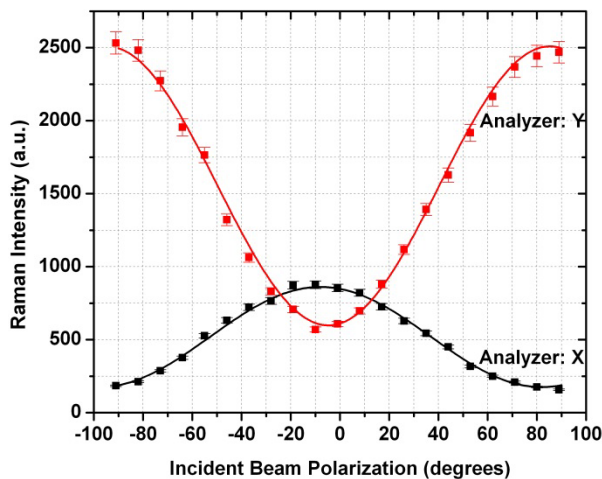


**Figure 5.** Raman intensity dependences on the polarization direction of the incident light for the X and Y analyzer positions measured at the point marked by a star in Figure 4(b). The error bars account for the  $\sim 3\%$  intensity variations of the incident laser light. The continuous curves represent fit functions based on Equation 4 used to obtain the three Euler angles:  $\alpha = 51^\circ \pm 2^\circ$ ,  $\beta = 27^\circ \pm 2^\circ$ , and  $\gamma = -2^\circ \pm 2^\circ$  necessary to determine the grain orientation and the stress tensor components.

Their fitting by the Equation 4 gives the following three Euler angles:  $\alpha = 51^\circ \pm 2^\circ$ ,  $\beta = 27^\circ \pm 2^\circ$ , and  $\gamma = -2^\circ \pm 2^\circ$ , which in turn provide the following rotation matrix to bring this arbitrary oriented grain in the stage (reference) coordinate system:

$$T(\alpha, \beta, \gamma) = \begin{pmatrix} 0.656 & -0.664 & 0.356 \\ 0.753 & 0.587 & -0.293 \\ -0.014 & 0.461 & 0.887 \end{pmatrix}.$$

Second, since the internal stresses are too small to produce a visible lifting of degeneracy of the three silicon optical phonon frequencies, the polarization settings for the incident and backscattered light for which the intensity of one of the three phonon modes dominates the other two are simulated using the previously determined Euler angles and Equation 5. The simulations of the six intensity ratio functions  $W^{xy}_j(\theta)$  are shown in Figure 6. It can be seen that the polarization settings to measure separately the three phonon frequency shifts  $\Delta\omega_j$  for the given grain are: Phonon 1:  $1^\circ$ , X, Phonon 2:  $-22^\circ$ , Y, and Phonon 3:  $15^\circ$ , Y.

Third, three Raman maps of the area in Figure 4(b) are measured for the three polarization settings above. Difference stress-tensors are calculated numerically from the three Raman frequency shifts  $\Delta\omega_j$  with respect to the stage (reference) coordinate system as described in Section 2.2:

$$\Delta\sigma_1 = \begin{pmatrix} -184 \pm 10 & -33 \pm 1 & 0 \\ -33 \pm 1 & -192 \pm 10 & 0 \\ 0 & 0 & -151 \pm 10 \end{pmatrix} MPa,$$

$$\Delta\sigma_2 = \begin{pmatrix} -200 \pm 10 & -51 \pm 1 & 0 \\ -51 \pm 1 & -213 \pm 10 & 0 \\ 0 & 0 & -152 \pm 10 \end{pmatrix} MPa.$$

The two lateral stress gradients indicate compressive stresses at these positions with respect to the point marked by the star in Figure 4(b), while the shift towards lower frequencies ( $\sim 520 \text{ cm}^{-1}$ ) in the position of the Raman spectra implies tensile stress inside the silicon thin film. Their conversion into average or von Misses stresses using Equation 9 gives  $\Delta\sigma_1=227$ ,  $\Delta\sigma_2=197 \pm 12.5 \text{ MPa}$ .

Figure 4(c) shows the asymmetry (doping) map obtained from the symmetry parameter  $q$  of the Raman spectra as defined in Section 2.3. For the quantitative doping evaluation, the free carrier concentration vs.  $q$  calibration curve in Figure 5 of Reference 11 was used. The free hole concentrations are found to be lower than the nominal boron doping of  $2.1 \times 10^{19}$  presumably due to the incomplete activation of dopants during laser crystallization and cooling [11]. Higher doping is observed both along GBs and inside grains. Regarding the influence of doping/impurities on the FWHM as discussed in Section 2.3, there is no correlation between them as seen by comparing the FWHM map with the asymmetry map displayed in Figure 4(a) and (c), respectively.

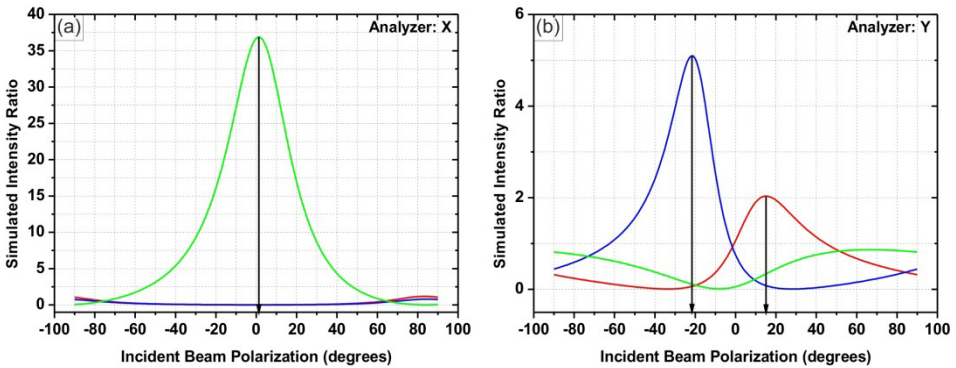


**Figure 6.** Simulation of the six intensity ratio functions  $W^{XY}_i(\theta)$  for the central grain in Figure 4(b). The plot maxima marked by arrows indicate the polarization direction of the incident laser light for the two analyzer positions where the intensity of one of the three silicon phonons dominates over the sum of the other two phonons.

The different Raman scattering efficiencies caused by distinct crystallographic grain orientations and the polarization directions of the incident and backscattered laser light can be used to image the grains and to determine their orientations as shown in Section 2.1. This results in intensity maps such as displayed in Figure 4(d), which enable tracing of GBs represented as solid lines in all Raman maps of Figure 4. Thus, it is possible to relate grains and GBs to defect, stress and doping distributions, all data being provided by the same Raman mapping.

#### 4.1.2. Wafer and ribbon-based silicon solar cells

Next examples illustrate the application of micro-Raman spectroscopy to block-cast and edge-defined film-feed (EFG) multicrystalline silicon materials, two industrial relevant materials with the former having the largest share (> 50%) in the PV market. Internal stresses are the result of the superposition between the thermally induced residual stresses that is the thermally induced stresses at the end of crystallization and cooling processes and the defect-related stresses. By cutting the silicon blocks and EFG tubes into wafers and then into small pieces for micrometer scale investigations, the thermally induced residual stresses are expected to relax to a large extent due to the creation of free surfaces. This is different in the case of silicon thin films on glass, which are measured as-prepared without any cutting. Thus, in the block-cast and EFG samples, the internal stresses produced mainly by defects are measured.

The resolution of micro-Raman can go down to single dislocation characterization as demonstrated in Figure 7(a) in the case of p-type block-cast mc-Si material taken from a PV factory production line. Here, the localized and quite symmetric stress distribution including both compressive (red area) and tensile (blue area) and its decay length resemble the stress field of an edge dislocation, which, in this case, is superimposed on the  $\Sigma 27a$  GB [23,27]. The polarized micro-Raman stress measurements give the following difference

stress tensors referring to the stage (reference) coordinate system shown in Figure 7(a). They have been evaluated between stressed positions close to the GB and positions at a distance from the GB, which are not affected by the dislocation stress field:

$$\Delta\sigma_1 = \begin{pmatrix} -40 \pm 10 & -14 \pm 3 & 0 \\ -14 \pm 3 & -38 \pm 10 & 0 \\ 0 & 0 & -25 \pm 10 \end{pmatrix} MPa,$$

$$\Delta\sigma_2 = \begin{pmatrix} 33 \pm 10 & -7 \pm 1 & 0 \\ -7 \pm 1 & 31 \pm 10 & 0 \\ 0 & 0 & 34 \pm 10 \end{pmatrix} MPa.$$

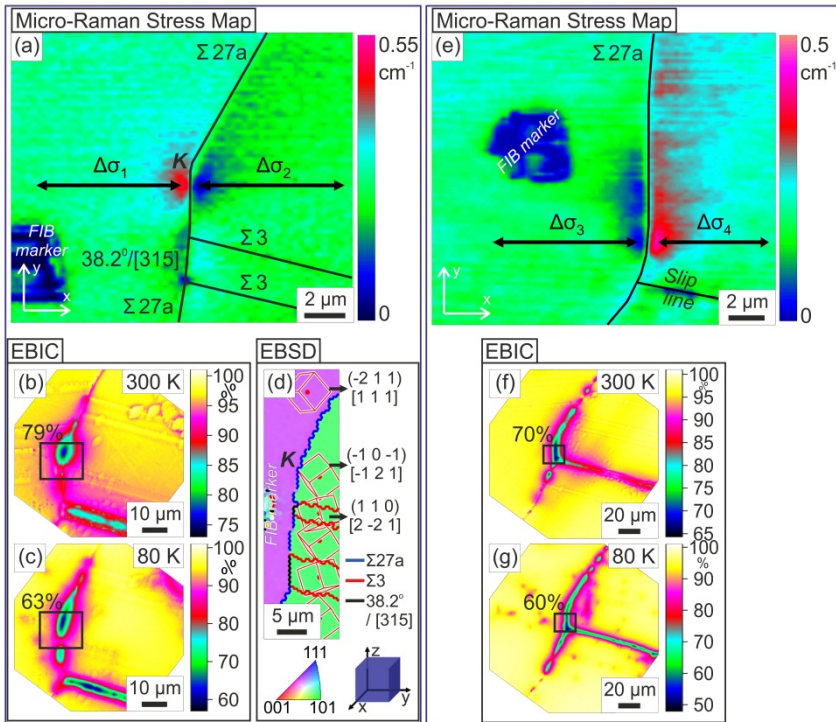
As shown in the previous example, it is worth to combine at the same position micro-Raman with other techniques not only to support the interpretation of the Raman results but also to get new insights into other material properties and their interplay. The EBIC images in Figure 7(b and c) show lower signal corresponding to reduced minority carrier lifetime of 79% at 300K and 63% at 80K in the region of the GB trajectory change where the edge dislocation is located as well as a signal variation along the  $\Sigma 27a$  GB. By comparing the stress and EBIC images, it can be seen that the stressed area close to the change in the  $\Sigma 27a$  GB trajectory denoted K and the stress-free area above and below it show similar EBIC signals, and thus similar recombination activities.

Figure 7(e) shows a Raman stress map of the same  $\Sigma 27a$  GB at a distance of several millimeters from the position displayed in Figure 7(a). The compressive (red area) and tensile (blue area) stresses are more extended along the GB, less symmetric, and change positions with respect to the GB as compared with the stress map in Figure 7(a). This stress distribution is attributed to the stress field of an array of edge dislocations superimposing the GB. The band-like less compressed region on the right-hand side of the  $\Sigma 27a$  GB can be explained by the presence of dislocations (edge, screw and/or mixed), in the grain and close to the GB, which have locally rearranged during crystal growth and cooling to reduce the strain energy and thus, the stresses in this region [23,27]. The following stress-tensor gradients referring to the stage (reference) coordinate system shown in Figure 7(e) have been determined by polarized micro-Raman:

$$\Delta\sigma_3 = \begin{pmatrix} 29 \pm 10 & -7 \pm 1 & 0 \\ -7 \pm 1 & 28 \pm 10 & 0 \\ 0 & 0 & 36 \pm 10 \end{pmatrix} MPa,$$

$$\Delta\sigma_4 = \begin{pmatrix} -34 \pm 10 & -3 \pm 1 & 0 \\ -3 \pm 1 & -37 \pm 10 & 0 \\ 0 & 0 & -37 \pm 10 \end{pmatrix} MPa.$$





**Figure 7.** Micro-Raman, EBIC and EBSD studies of block-cast solar silicon at two positions along the same  $\Sigma 27a$  GB. The Raman stress distributions are attributed to a single edge dislocation (a) and to an array of edge dislocations (e) superimposing the GB. The regions enclosed by rectangles in the EBIC images (b, c) and (f, g) correspond to the Raman mapped areas in (a) and (e), where the numbers indicate the maximum EBIC signal. The lower the EBIC signal, the higher the recombination activity. The focused ion beam (FIB) markers in (a, e) allows exact spatial correlation between different measurement techniques. (d) EBSD map showing the grain orientations and GB types along with the orientation triangle and the sample reference frame.

Like in the previous case the stressed and stress-free areas around the GB in Figure 7(e) are located in a region of similar (lower) EBIC signal of 70% at 300K and 60% at 80K as indicated in Figure 7(f) and (g), respectively and the recombination activity is inhomogeneous along the  $\Sigma 27a$  GB. These two representative examples demonstrate the presence of spatial variations in mechanical and electrical properties of block-cast solar silicon on the micrometer scale.

Similar spatial properties variations are observed in the p-type EFG mc-Si material taken also from a PV factory production line. In order to illustrate the correlation between internal stresses, defect structure and electrical activity in the EFG material, we show here three positions along the same GB that contain representative examples of this correlation. Here, the internal stresses are evaluated using Equation 11 without employing the polarized micro-Raman procedure as in the case of silicon thin films on glass and block-cast mc-Si.

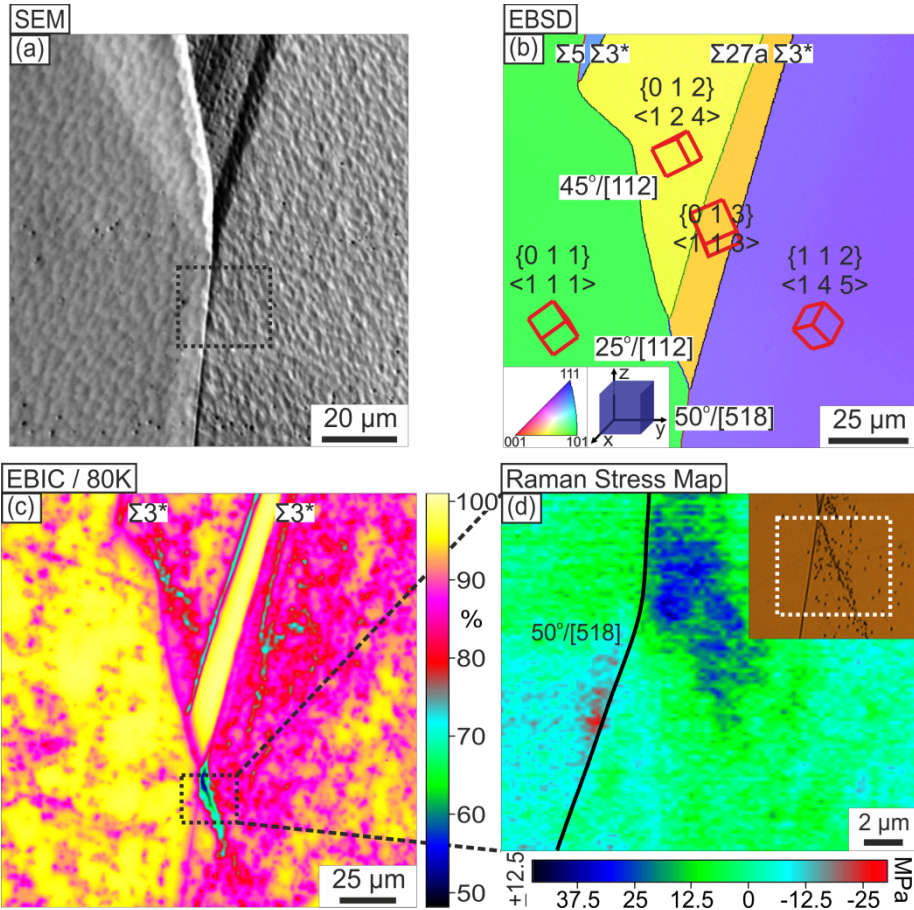


**Figure 8.** Position 1 (a) SEM image of the as-grown EFG wafer before mechanical polishing. (b) EBSD map showing the grain orientations and GB types along with the orientation triangle and the sample reference frame. (c) EBIC image taken at 80K where the inhomogeneous recombination activity inside grains and at GBs is mainly attributed to dislocations decorated with metallic impurities. (d) Not all dislocations visible in the defect etching image shown in the inset or measured by EBIC are accompanied by internal stresses as probed by micro-Raman. The dashed rectangle in the inset represents the Raman mapped area. At this position, the lowest EBIC current corresponds to the largest (tensile) stress.

The EBSD, EBIC, and micro-Raman measurements at the first position are displayed in Figure 8. The Raman stress map shows concentrated tensile (in blue) and compressive (in red) stresses close to a large-angle random GB described by a misorientation angle/axis of  $50^\circ/[518]$ . Except these areas, nearly no stresses are found neither along the GB nor inside the two adjacent grains of  $\{011\}\langle 111 \rangle$  and  $\{112\}\langle 145 \rangle$  orientations. By comparing the stress map with the corresponding EBIC map enclosed by the rectangle in Figure 8(c), it can be seen that not all recombination active dislocations visible at 80K are accompanied by stresses.

That is because dislocations interact with each other and tend to locally rearrange in configurations of minimum strain energy that can result in stresses or virtually no stresses. The EBIC image in Figure 8(c) shows an inhomogeneous electrical activity along different types of GBs as well as inside grains of different crystallographic orientations indicated in Figure 8(b). The recombination-active  $\Sigma$  GBs  $\{60^\circ/[111]\}$  in Figures 8-10 are marked with an asterisk to distinguished them from the recombination-free  $\Sigma$  GBs in Figure 9.

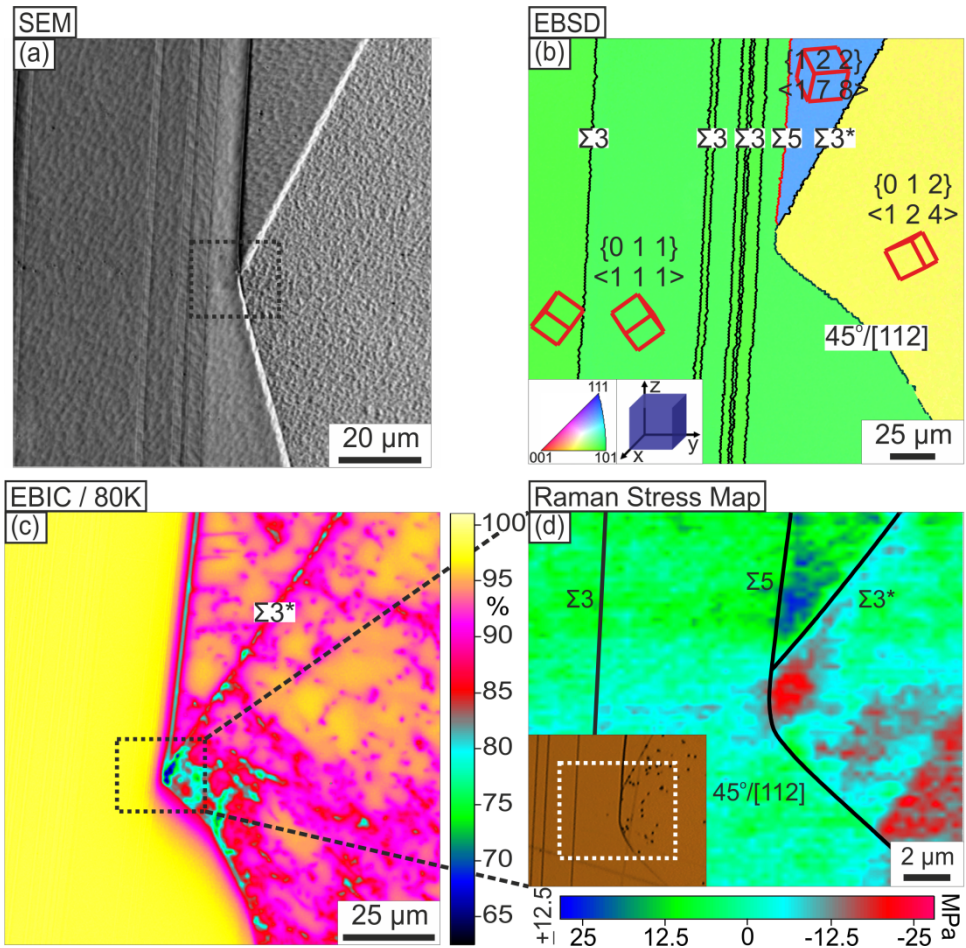


**Figure 9.** Position 2 (a) SEM image of the as-grown EFG water before mechanical polishing. (b) EBSD map. (c) EBIC image where the same left-hand side grain like in Figure 8 shows at this position no electrical activity. The  $\Sigma 3$  GBs are either recombination-free ( $\Sigma 3$ ) or recombination-active ( $\Sigma 3^*$ ), while being virtually stress-free. (d) The defect etching image in the inset indicates that the presence of dislocation etch pits on  $\Sigma 3^*$  GBs leads to electrical activity provided the dislocations are decorated with metallic impurities. Here, the highest recombination activity corresponds to the largest (compressive) stress.

The EBSD, EBIC, and micro-Raman results obtained at the second position are shown in Figure 9. Like in the previous case, we did not find a one-to-one correspondence between electrically active dislocations and stresses, both exhibiting inhomogeneous spatial and magnitude distributions. These findings are similar to those on block-cast mc-Si displayed in Figure 7. Different at this position is the presence of tensile (in blue) and compressive (in red) stresses concentrated close to a GB triple point where a  $\Sigma 5$  GB  $\{36.86^\circ/[100]\}$ , a  $\Sigma 3$  GB, and a large-angle random GB  $\{45^\circ/[112]\}$  meet. It is worth noting that GBs of the same type, here  $\Sigma 3$  GBs, can be either recombination-free ( $\Sigma 3$ ) or recombination active ( $\Sigma 3^*$ ), while being both nearly stress-free. Essentially, independent of the GB type, such large differences in electrical activity originate mainly from the absence or presence of recombination-active dislocations on or very close to the GB. This point is confirmed by comparing the defect-etched optical image with the EBIC map: the  $\Sigma 3$  GBs decorated by dislocation etch pits (denoted  $\Sigma 3^*$ ) show increased electrical activity, while the  $\Sigma 3$  GBs without dislocation etch pits show no recombination activity. It can be seen that despite the same GB type assignment by the EBSD software, the  $\Sigma 3^*$  and  $\Sigma 3$  GBs are formed between adjacent grains of different crystallographic orientations. This fact suggests distinct kinematic conditions at these  $\Sigma 3$  GBs that can lead to dissimilar thermally induced stress levels and as a result to the generation or absence of dislocations. On the other hand, Raman measures only those configurations of dislocations (including the recombination-free dislocations) that lead to stresses. In contrast with the first (Figure 8) and third (Figure 10) positions, the  $\{011\}\langle 111\rangle$  left-hand side grain shows no reduction of the EBIC signal at the second position despite quite similar grain geometries at these three positions. This indicates that the thermally induced stresses present during the EFG growth relaxed not through the generation of dislocations but through the formation of twins found at the second position by EBSD.

Similar to the previous two cases, we observe non-uniform distributions of electrical activity and stresses along GBs and inside grains at the third position as displayed in Figure 10(c, d). However, we choose this position to show that the largest recombination activity is not always accompanied by the largest internal stresses as in the case of the first and second positions.

The local variations in the sign and values of the dislocation-related stresses as well as in the strength of the recombination activity are attributed to the cumulative effect of metallic impurity decoration, intrinsic structure, type, density, and distribution of dislocations inside grains and on GBs. This non-uniform distribution of dislocations originates from locally different mechanisms of nucleation, motion, multiplication and annihilation of dislocations controlled by the grain structure including the orientation, size and geometry of the grains, the kinematic constraints at GBs, and temperature. The presence of impurities is confirmed by EBIC measurements which show quite strong reduction of the EBIC signal at room temperature up to 70-80% which further reduces with decreasing temperature up to 50-65% at 80K. Such EBIC behavior corresponding to increasing recombination can be explained by the interaction of shallow levels related to the strain fields of dislocations with deep levels due to metallic impurity decoration and/or intrinsic core defects at dislocations. It is known that impurity accumulation in silicon can be enhanced due to the presence of stresses

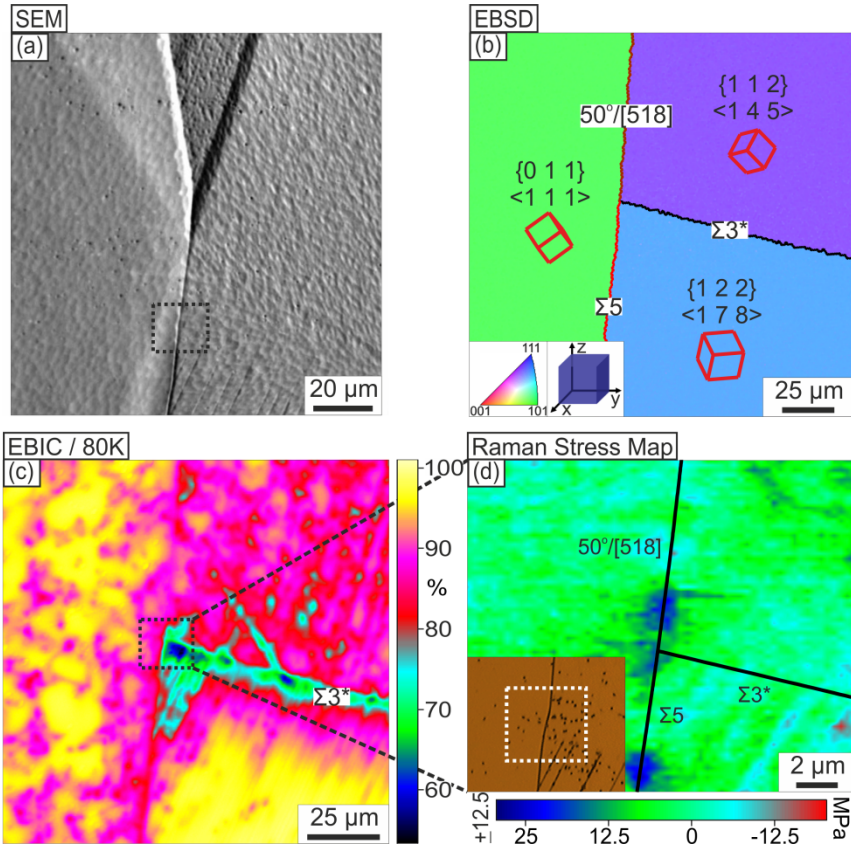


**Figure 10.** Position 3 (a) SEM image of the as-grown EFG wafer before mechanical polishing. (b) EBSD map. (c) EBIC image where the same left-hand side grain like in Figure 8 and 9 shows recombination activity. (d) The lowest EBIC current is not accompanied by stress at this position.

(thermally induced residual stresses and/or defect-related stresses) at temperatures where both impurities and dislocations are mobile. This can explain the increased electrical activity at regions of higher dislocation densities as at the first and second positions where dislocations are spatially distributed in such a way that their stress fields cancel partially or not at all so that an overall long-range stress field from these dislocations is measured by micro-Raman. The dislocations arranged in configurations in which their stress fields cancel totally (or below the detection limit of our Raman spectrometer of  $\pm 12.5$  MPa) are only visible by EBIC (when recombination-active) but not by micro-Raman, as at the third position. Point-by-point correlation of the micro-Raman and EBIC measurements indicates that internal stresses of several tens of MPa do not influence the minority carrier recombination in block-cast and EFG mc-Si. Comparably high stresses of up to 1.2 GPa are necessary in silicon in order to influence its electrical properties such as enhanced carrier mobility in the transistor channel through band structure modification and effective mass reduction [6,23].

## 4.2. Macro-Raman measurements

Representative macro-Raman mappings acquired using the DuoScan option described in Section 3.3 on the laser crystallized silicon seed layers of thin film solar cells on glass (in this example, 290 nm thick silicon seed film) are displayed in Figure 11. These measurements are performed at identical positions using probing macro-beams of  $30 \times 30 \mu\text{m}^2$  and  $100 \times 100 \mu\text{m}^2$  with the 50x and 10x NIKON microscope objectives. The distribution of internal stresses (a, c) and defect densities (b, d) obtained from the position and FWHM of the measured Raman spectra are quite similar when measuring with different DuoScan macro-beam sizes. The inhomogeneous stress patterns in (a, c) are the result of the interaction between defects through their own intrinsic stress fields and thermally induced residual stresses, while the line shape regions in (b, d) correlate with the laser traces where higher defect densities corresponding to larger FWHM values develop predominantly at adjacent laser scan lines where irradiated areas overlap. It can be seen that there is no correlation between the shift/position (stress) and FWHM (defect density) maps both at macro-scale (Figure 11(a-d)) as well as at micro-scale (Figure 4(a and b)). This further supports the argument used to explain the results in the previous sections, namely the locally different interaction between dislocations themselves and with thermally induced residual stresses.

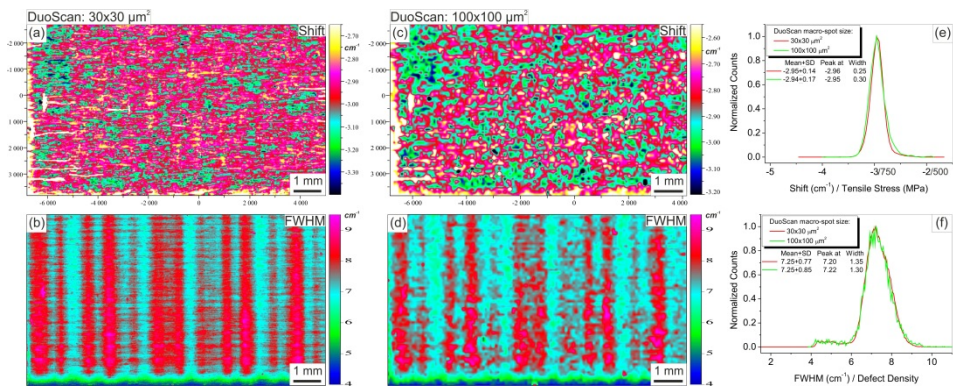


**Figure 11.** DuoScan Raman maps of the same area using probing macro-beams of  $30 \times 30 \mu\text{m}^2$  (a, b) and  $100 \times 100 \mu\text{m}^2$  (c, d), where the sharpness of the features decreases due the loss of lateral resolution. (a, c) The Raman peak position shifts with respect to a stress-free silicon reference are negative indicating the presence of tensile stresses inside the 290 nm thick laser crystallized silicon thin film on glass. (b, d) The FWHM maps show areas of different crystal quality related to different defect densities, which correlate with the laser traces as visible from the line shape character of the FWHM distributions. (e, f) Statistical evaluation using histograms for the two macro-beam sizes demonstrating that DuoScan can be used for large scale mappings without losing average information.

As expected, the sharpness of the features decreases with increasing the size of the probing macro-beam due the loss of lateral resolution. However, the spectral information is not altered by integrating the Raman signal over the  $30 \times 30 \mu\text{m}^2$  or  $100 \times 100 \mu\text{m}^2$  macro-beam areas. Indeed, the normalized histograms in Figure 11(e, f) calculated from the shift and

FWHM DuoScan maps show a good overlap demonstrating that DuoScan can be used for large-scale mapping of PV and other Raman active materials without losing average spectral information. The presence of thermally induced residual stresses is reflected in the position of the shift/stress histogram in Figure 11(e). Smaller thermally induced residual stresses corresponding to shift/stress histograms closer to or at zero prevent cracking or peeling off the silicon thin film solar cells or even substrate bending minimizing the breakage risk and processing/handling difficulties. When small, they also impede under external mechanical and thermal loads the occurrence of new stress-induced defects, which are commonly recombination active. The qualitative estimation of defects is apparent in the position of the FWHM/defect density histogram in Figure 11(f) where FWHM values closer to  $\sim 3 \text{ cm}^{-1}$  corresponding to defect-free silicon indicate lower defect densities in the silicon thin film solar cells. Thus, macro-Raman can be used to evaluate statistically the materials properties and to see clearly the changes originating from different preparation conditions and processing.

## 5. Conclusions

The characterization power of the Raman technique at micro- and macro-scale in the case of multicrystalline solar silicon materials is demonstrated. Raman investigations at length scales ranging from  $\mu\text{m}^2$  to  $\text{cm}^2$  are possible through two new developed scanning modules, DuoScan™ (hardware) and SWIFT™ (software), which can be integrated in any standard micro-Raman spectrometer. The statistical evaluation of the large area Raman maps measured by macro-Raman spectroscopy shows that macro-scale Raman mapping integrates data over the macro-beam area giving an average spectrum that contains the full spectral information at the cost of decreasing lateral resolution. Moreover, Macro-Raman enables significant reduction by orders of magnitude of the acquisition time: if an area of  $30 \times 30 \mu\text{m}^2$  is entirely probed by macro-Raman in one second, micro-Raman with a spot-size of  $1 \times 1 \mu\text{m}^2$  needs 900 seconds to cover the same area. Deeper insights into the interplay between internal stresses, defects, doping, microstructure, and recombination activity with practical impact on the mechanical stability and conversion efficiency of solar cells have been obtained by combining Raman, EBSD, EBIC, TEM, and defect etching techniques. By tuning the crystallization process, the interaction between dislocations driven by the strain energy minimization can be used to reduce internal stresses resulting in mechanically stronger wafers and cells and to prevent metallic impurity precipitation at dislocations that should lead to improved energy conversion efficiencies.

## Author details

George Sarau and Silke Christiansen

*Max Planck Institute for the Science of Light, Erlangen, Germany*

*Institute of Photonic Technology, Jena, Germany*

Arne Bochmann

*Institute of Photonic Technology, Jena, Germany*

Renata Lewandowska  
*Horiba Scientific, Villeneuve d'Ascq, France*

## Acknowledgement

This work was financially supported by (1) the German Federal Ministry for the Environment, Nature Conservation and Nuclear Safety and all the industry partners within the research cluster "SolarFocus", (2) the Max-Planck Society within the project "Nanostress", and (3) the European Commission within the FP7-Energy priority project "High-EF". Within the "High-EF" project, Horiba Scientific developed the DuoScan hardware and the SWIFT software that permit fast, large area Raman analyses. The first demonstrator was deployed to the Max Planck Institute for the Science of Light for further development of this technique with respect to applications in photovoltaics. The authors are thankful for this great research opportunity. We would also like to thank A. Gawlik of IPHT for preparing the laser crystallized samples used in this study as well as to M. Holla and W. Seifert of Joint Lab IHP/BTU for their help with the EBIC measurements and fruitful discussions. The content of this publication is the responsibility of the authors.

## 6. References

- [1] Raman C.V, Krishnan K.S (1928) A New Type of Secondary Radiation. *Nature* 121: 501-502.
- [2] Ferraro J.R, Nakamoto K, Brown C.W (2003) *Introductory Raman Spectroscopy*. Academic Press.
- [3] Smith E, Dent G (2005) *Modern Raman Spectroscopy - A Practical Approach*. John Wiley & Sons.
- [4] Pelletier M.J (Ed.) (1999) *Analytical Applications of Raman Spectroscopy*. Blackwell Publishing.
- [5] Wolf I (1996) Micro-Raman Spectroscopy to Study Local Mechanical Stress in Silicon Integrated Circuits. *Semicond. Sci. Technol.* 11: 139-154.
- [6] Sarau G, Christiansen S, Holla M, Seifert W (2011) Correlating Internal Stresses, Electrical Activity and Defect Structure on the Micrometer Scale in EFG Silicon Ribbons. *Sol. Energy Mater. Sol. Cells* 95: 2264–2271.
- [7] Sarau G, Christiansen S, Lewandowska R, Roussel B (2010) Future of Raman in PV Development. *Proc. 35th IEEE PVSC*: 001770-001775.
- [8] Anastassakis E, Pinczuk A, Burstein E, Pollak F.H, Cardona M (1970) Effect of Static Uniaxial Stress on the Raman Spectrum of Silicon. *Solid State Commun.* 8: 133-138.
- [9] Wolf I, Maes H.E, Jones S.K (1996) Stress measurements in silicon devices through Raman spectroscopy: Bridging the gap between theory and experiment. *J. Appl. Phys.* 79: 7148-7156.



- [10] Becker M, Scheel H, Christiansen S, Strunk H.P (2007) Grain orientation, texture, and internal stress optically evaluated by micro-Raman spectroscopy. *J. Appl. Phys.* 101: 063531 (1-10).
- [11] Becker M, Gösele U, Hofmann A, Christiansen S (2009) Highly p-doped Regions in Silicon Solar Cells Quantitatively Analyzed by Small Angle Beveling and micro-Raman Spectroscopy. *J. Appl. Phys.* 106: 074515 (1-9).
- [12] Anastassakis E (1999) Strain Characterization of Polycrystalline Diamond and Silicon Systems. *J. Appl. Phys.* 86: 249-258.
- [13] Puech P, Pinel S, Jasinevicius R.G, Pizani P.S (2000) Mapping the three-dimensional strain field around a microindentation on silicon using polishing and Raman spectroscopy. *J. Appl. Phys.* 88: 4582-4585.
- [14] Hanbücken M, Müller P, Wehrspohn R.B (Eds.) (2011) *Mechanical Stress on the Nanoscale: Simulation, Material Systems and Characterization Techniques*. Wiley-VCH.
- [15] Fano U (1961) Effects of Configuration Interaction on Intensities and Phase Shifts. *Phys. Rev.* 124: 1866- 1878.
- [16] Nickel N.H, Lengsfeld P, Sieber I (2000) Raman Spectroscopy of Heavily Doped Polycrystalline Silicon Thin Film. *Phys. Rev. B* 61: 15558-15561.
- [17] Lengsfeld P, Brehme S, Brendel K, Genzel Ch, Nickel N.H (2003) Raman Spectroscopy of Heavily Doped Polycrystalline and Microcrystalline Silicon. *phys. stat. sol. (b)* 235: 170-178.
- [18] Weber W.H, Merlin R (Eds.) (2000) *Raman Scattering in Materials Science*. Springer. pp. 56-64.
- [19] Debernardi A, Baroni S, Molinari E (1995) Anharmonic Phonon Lifetimes in Semiconductors from Density-Functional Perturbation Theory, *Phys. Rev. Lett.* 75: 1819-1822.
- [20] Debernardi A (1998) Phonon linewidth in III-V semiconductors from density-functional perturbation theory, *Phys. Rev. B* 57: 12847.
- [21] Iqbal Z, Veprek S, Webb A.P, Capezzuto P (1981) Raman Scattering from Small Particle Size Polycrystalline Silicon, *Solid State Commun.* 37: 993-996.
- [22] Secco D' Aragona F (1972) Dislocation Etch for (100) Planes in Silicon, *J. Electrochem. Soc.* 119: 948-951.
- [23] Sarau G, Becker M, Christiansen S, Holla M, Seifert W (2009) Micro-Raman Mapping of Residual Stresses at Grain Boundaries in Multicrystalline Block-Cast Silicon Solar Cell Material: Their Relation to the Grain Boundary Microstructure and Recombination Activity, *Proc. 24th European Photovoltaic Solar Energy Conference*: 969-973.
- [24] Sarau G, Becker M, Berger A, Schneider J, Christiansen S (2007) Stress Distribution in Polycrystalline Silicon Thin Film Solar Cells on Glass Measured by Micro-Raman Spectroscopy, *Mater. Res. Soc. Symp. Proc.* 1024E: 1024-A07-04.

- [25] Grimmer H, Bollmann W, Warrington D.H (1974) Coincidence-Site Lattices and Complete Pattern-Shift in Cubic Crystals, *Acta Cryst.* A30: 197-207.
- [26] Niederberger Ch, Michler J, Jacot A (2008) Origin of Intragranular Crystallographic Misorientations in Hot-Dip Al-Zn-Si Coating, *Acta Materialia* 56: 4002-4011.
- [27] Hull D, Bacon D.J (2001) *Introduction to Dislocations*. Butterworth-Heinemann. Chapters 4 and 9.